Supplementary Materials

Samples

In the present study two CsV_3Sb_5 samples grown in different laboratories were measured in two Sagnac interferometers. First samples dubbed "sample 1" is from Cluadia Felser group in Dresden, it was measured in Kapitulnik group at Stanford, second sample dubbed "sample 2" grown at Stephen D. Wilson's group at UCSB was studied at UC Irvine in Xia group.

Sample mounting

We thermally and mechanically anchor samples to copper coldfinger using either Leitsilber 200 silver paint or thin layer of VGE-7031 varnish. To ensure that the results of our study are robust against the strain imposed by the mismatch of thermal expansion coefficients between the sample and the coldfinger, we repeat all the measurements in two different configurations (Fig. 1).

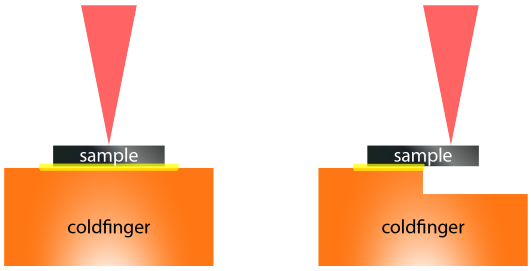

FIG. 1: **Sample mounting.** Two different ways used to glue sample to the coldfinger.

Zero-area-loop Fiber-optic Sagnac Interferometer (ZALSI)

Samples were measured using zero loop area fiber Sagnac interferometers (ZALSI) [1] using 30 μW optical power at 1550 nm wavelength with phase modulation at $\omega = 5$ MHz. Two low-coherence light waves of right and left circularly polarizations were sent to the sample. And the non-reciprocal phase difference $\varphi_{nr} = 2\theta_K$ between the two lights acquired upon reflection was detected with lock-in amplifiers. By construction, unlike a standard ellipsometer, this approach fundamentally rejects polarization rotations due to non-TRSB effects such as linear and circular birefringence and dichroism that could mimic a TRSB Kerr signal. In addition, by reducing the Sagnac loop to zero area within a single fiber, it also rejects a background Sagnac signal from earth rotation, which breaks time-reversal symmetry and is the basis for fiber gyroscopes.

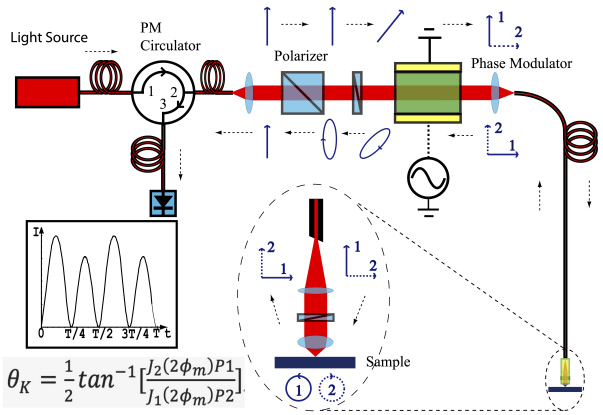

FIG. 2: **ZALSI.** Schematics of the zero-area-loop fiber-optic Sagnac interferometer (ZALSI).

The apparatus is based on the Sagnac interferometer [2] where two counter-propagating beams travel the exact same optical path before interfering at the detector. In our implementation we use two orthogonally linearly polarized light beams, which are then converted into right and left circular polarizations using a quarter-wave plate. An objective lens focuses the light onto a small interaction region on the sample, and the reflected light beams are converted back to linear polarizations with exchanged polarization directions. Owing to the reciprocity of the apparatus, a non reciprocal phase shift $\phi_{nr} = 2\theta_K$ will appear at the detector only if time reversal symmetry is broken through the interaction of the two circularly polarized beams with the sample [1]. With careful construction we can routinely achieve shot-noise-limited senstivity of ($\sim$100 nrad/$\sqrt{Hz}$) for optical power above $\sim$ 10 μW, with magneto-optic Kerr and Faraday resolutions of nrad limited by the long-term drift of the instrument. Some of our notable accomplishments include the study of TRSB in Sr_2RuO_4 [3], UPt_3 [4] and more recently UTe_2 [5, 6], elucidating the limit for ferromagnetism in thin $SrRuO_3$ films [7] and discovery of the inverse proximity effect in ferromagnet/superconductor bilayers [8] to name a few. Again, to be able to reliably scrutinize the possible spontaneous polar Kerr effect below T^*, measurements were performed in two different apparatuses, one at Stanford University and one at UC Irvine. While both systems were constructed in a similar way employing a broadband superluminescent light emitting diode (SLED) with a center wavelength of 1550 nm, the details of the sample holder, windows construction and end-optics are slightly different.

A schematics of ZALSI as well as polarization states at each point are shown in Fig. 2. The beam of light polarized at 45° to the axis of a electro-optic modulator

(EOM), which generates 5 MHz time-varying differential phase shifts ϕ_m along its two major axis and split the light into two beams of roughly equal powers. The two beams are then launched into the fast and slow axes respectively of a polarization maintaining (PM) fiber. Upon exiting the fiber, the two orthogonally polarized beams are converted into right- and left-circularly polarized light by a quarter-wave ($\lambda/4$) plate, and are then focused onto the sample. The non-reciprocal phase shift ϕ_{nr} between the two circularly polarized beams upon reflection from the sample is twice the Kerr rotation ($\varphi_{nr} = 2\theta_K$). The same quarter-wave plate converts the reflected beams back into linear polarization, but with a net 90^o rotation of the polarization axis. The two beams then travel back through the PM fiber and the EOM with exchanged axes before they arrive again at the polarizer. At this point, the two beams have gone through exactly the same path but in opposite directions, except for a phase difference of $\phi_{nr} = 2\theta_K$ from reflection off of the sample. The two beams are once again coherent, and interfere to produce an elliptically polarized beam, whose in-plane component is routed by the circulator to the photodetector. Lock-in detection was used to measure the average (DC) power (P_0), the first harmonics (P_1), and the second harmonics (P_2) of the detected optical power $P(t)$:

$$P(t) = \frac{1}{2}P[1 + \cos(\varphi_{nr} + 2\phi_m \sin(\omega t))] \tag{A.1}$$

where P is the returned power without modulation, and depends on focus of the objective lens and sample reflectivity. $P(t)$ can be further expanded into Fourier series of ω if we keep φ_{nr} as a slowly time-varying quantity compared to ω:

$$\begin{aligned} P(t)/P = {} & [1 + J_0(2\phi_m)]/2 \\ & +(\sin(\varphi_{nr})J_1(2\phi_m))\sin(\omega t) \\ & +(\cos(\varphi_{nr})J_2(2\phi_m))\cos(2\omega t) \\ & +2J_3(2\phi_m)\sin(3\omega t) \\ & +... \end{aligned} \tag{A.2}$$

where J_1 and J_2 are Bessel functions. Therefore, the detected powers P_0, P_1 and P_2 are:

$$P_0/P = [1 + J_0(2\phi_m)]/2, \tag{A.3}$$

$$P_1/P = (\sin(\varphi_{nr})J_1(2\phi_m)), \tag{A.4}$$

$$P_2/P = (\cos(\varphi_{nr})J_2(2\phi_m)) \tag{A.5}$$

Hence Kerr signal $\theta_K = \varphi_{nr}/2$ can be obtained using equation A.6, which is independent of optical power, sample reflectivity and focus of the objective lens. For optimal θ_K sensitivity ϕ_m is often chosen to be close to 0.92.

$$\theta_K = \frac{1}{2}\tan^{-1}\left[\frac{J_2(2\phi_m)P_1}{J_1(2\phi_m)P_2}\right] \tag{A.6}$$

Time-reversal Symmetry Preserving design

Here we provide a qualitative argument on why ZALSI only detects a signal when TRS is broken. Assume a sample with its surface in the x-y plane and a linearly polarized electric field propagating along the z-direction which is perpendicular to the surface of the sample. Adopting the common convention where the sense of circular polarization is determined with respect to a fixed axis (here the $+z$ axis), the handedness of the reflected light with respect to the direction of propagation flips. This convention defines four different indices of refraction: $n_{R\nearrow}$ and $n_{L\nearrow}$ are the refractive indices for right circularly polarized (RCP) light and left circularly polarized (LCP) light propagating along $+z$ (reflected light) and $n_{R\searrow}$ and $n_{L\searrow}$ are the refractive indices for RCP and LCP propagating along $-z$ (incident light). Where TRS is preserved

$$\begin{aligned} n_{R\nearrow} &= n_{L\searrow}, \\ n_{L\nearrow} &= n_{R\searrow}, \end{aligned} \tag{A.7}$$

however, if TRS is broken at least one equality in (A.7) fails. Focusing on a polar configuration where light impinges on the sample at normal incidence (as it is in our ZALSI apparatus) and using scattering theory to calculate the Kerr effect from the difference between the reflection amplitudes for right and left circularly polarized light [9], it can be shown that

$$\theta_K \propto [(n_{R\nearrow} + n_{R\searrow}) - (n_{L\nearrow} + n_{L\searrow})]. \tag{A.8}$$

It is then clear that θ_K is finite *only* for the case of TRSB. The above results are robust, independent of whether the material that we study is isotropic, or it possesses linear birefringence or natural optical activity.

Detection of CDW with coherent reflection ratio P_2/P_0

In addition to the Kerr signal, we record the total (P0) and the coherence (P2) parts of the reflected optical power, as their ratio serves as a measure of the linear and/or circular birefringence. The above calculations of the ZALSI assume perfect retardance of the quarter-wave plate and absence of either linear or circular birefringence and dichroism of the sample. In reality, commercial zero-order quarter-wave plates have a typical retardance error of 1% even for normal incidence, and samples such as CsV_3Sb_5 display birefringence and/or dichroism. As a result, the reflected beams, after passing the quarter-wave plate again, become elliptical instead of being perfectly linearly polarized. And a small fraction of the light will be incoherent with the major beams and thus won't participate in the interference. These incoherent components will not be captured by P_1 or P_2, but will still be detected as part of the average power P_0.

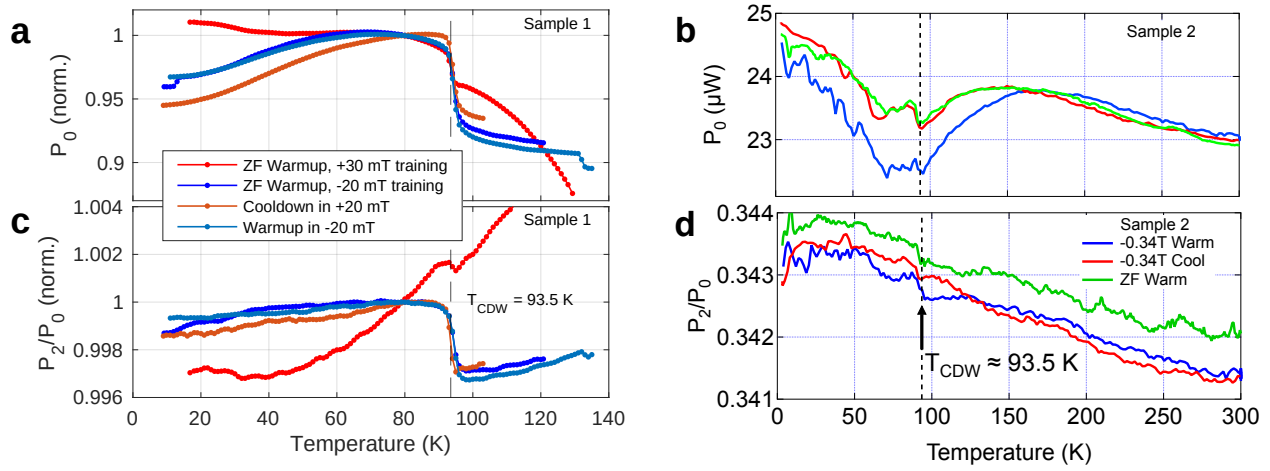

FIG. 3: **Birefringence and dichroism in CsV_3Sb_5 detected by Sagnac interferometers**. **a**, Normalized average (DC) power P_0 in sample 1. **b**, Average (DC) power P_0 in Sample 2. **c**, Coherent reflection ratio P_2/P_0 in sample 1. **d**, P_2/P_0 in sample 2. The abrupt change of P_2/P_0 at $T^* \approx 94$ K in both samples indicate the onset of birefringence and/or dichroism (linear or circular) in CsV_3Sb_5 .

And pre-factors need to be added to the formulas for P_0, P_1 and P_2:

$$P_0/P = (1 + A_0)[1 + J_0(2\phi_m)]/2, \tag{B.1}$$
$$P_1/P = (1 + A_1)(\sin(\varphi_{nr})J_1(2\phi_m)), \tag{B.2}$$
$$P_2/P = (1 + A_2)(\cos(\varphi_{nr})J_2(2\phi_m)) \tag{B.3}$$

where A_0, A_1 and A_2 are small correction pre-factors for sample birefringence and/or dichroism, and retardance error of the wave plate. The Kerr signal θ_K can be obtained using updated equation B.4, with a small correction to the scaling factor. There is no change to the zero point of θ_K, which is guaranteed by the symmetry of the interferometer.

$$\theta_K = \frac{1}{2}\tan^{-1}\left[\frac{(1 + A_2)J_2(2\phi_m)P_1}{(1 + A_1)J_1(2\phi_m)P_2}\right] \tag{B.4}$$

On the other hand, a change in sample birefringence and/or dichroism will induce changes to P_0 and P_2. However, as previously mentioned, they are also dependent on P, which changes with focus of the objective lens and sample reflectivity.

$$P_2/P_0 = \frac{(1 + A_2)J_2(2\phi_m)}{(1 + A_0)(1 + J_0(2\phi_m))} \tag{B.5}$$

Their ratio P_2/P_0 is independent of these factors and represents the ratio between the coherent and the total optical powers, dubbed "coherent reflection ratio". Since the wave plate retardance error is a slow varying quantity usually dominated the slow drifts of its tilt and rotation, P_2/P_0 can be used to measure that change of sample birefringence and/or dichroism during temperature sweeps.

Experimental Details

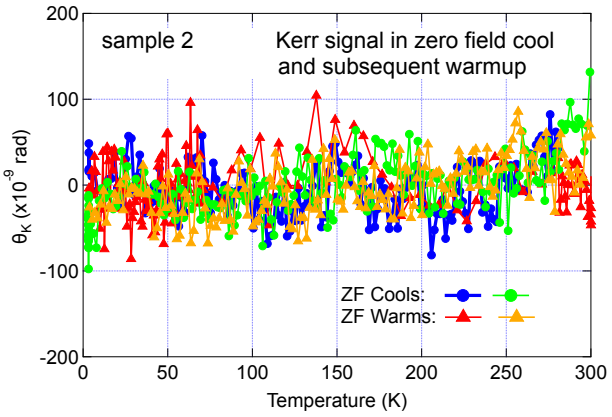

FIG. 4: **Zero-field cool.** Kerr signal during zero-field cools and subsequent warmups in sample 2 measured at Irvine, showing no spontaneous Kerr signal above 30 nrad.

In a typical experiment, we align the focused beam to an optically flat area of the crystal after cleaving. This can be facilitated by scanning imaging as shown in Fig. 5 for sample 2, where a flat region of 300 μm in size can be identified with high reflectivity (P0 of 10 to 30 μW) at T = 3.1 K. Kerr signals are obtained in the same scan. At B = - 0.34 T, a uniform Kerr signal of - 8.16 μrad is observed, even though the reflected light varies by 300% across the region. And upon removing the magnetic field, the Kerr signal is reduced to zero without any sign of spontaneous TRSB. The optical beam is then fixed at

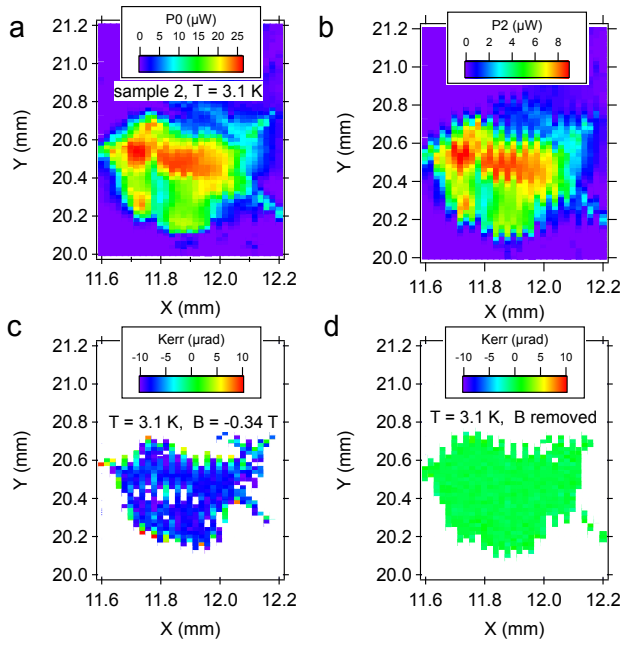

FIG. 5: **Sagnac scanning images.** Sample 2 measured at Irvine. **a**, P0 and **b**, P2 are detected DC and second harmonics optical powers taken at T = 3.1 K sample temperature, showing an optically flat region colored in red to green. **c**, Kerr image taken at T = 3.1 K and in a magnetic field of B = -0.34 T, showing a uniform Kerr signal of - 8.16 μrad (-24 μrad/T). **d**, Kerr image taken after the magnetic field is removed, showing zero spontaneous Kerr signal.

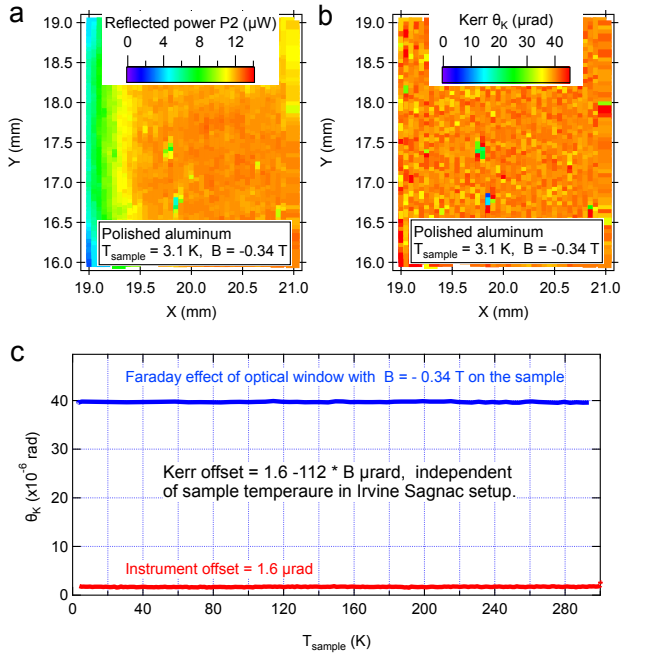

FIG. 6: **Calibration of background offsets.** Window calibration of Irvine Sagnac setup. (A) P2 and (B) Kerr images of a polished aluminum surface measured at T = 3.1 K and B =-0.34 T, showing a uniform background Kerr signal of 39.7 μrad from the optical window, even when P2 varies between 7 to 12 μW across the imaged region. (C) This 39.7 μrad optical window background (blue) as well as an instrument offset of 1.6 μrad are both independent of sample temperature. The total calibrated offset is 1.6 - 112 B μrad.

a location temperature sweeps, as presented in Fig. 2 of the main text. During zero magnetic field warmups, an absolute Kerr resolution of 30 nrad is typically achieved over a wide temperature range between 0 and 300 K. For a smaller temperature range of a few K, we can detect a change of Kerr signal as small as 10 nrad.

To reveal the diamagnetic shift below $T_{\rm CDW} = 93.5K$, it is necessary to perform Sagnac measurements when the sample is subject to a magnetic field. In our normal Sagnac setups[3], the fiber-optic head containing the wave-plate and focusing lens are placed inside the cryostat to achieve the lowest sample temperatures. Under a magnetic field, the fiber-optic head will contribute its own temperature-dependent Kerr signal, about 50 μrad/T at room temperature and 100 μrad/T below 4 K. Due to the long thermalization time of glass at cryogenic temperatures, the temperature of the fiber-optic head often deviates significantly from the sample temperature readings, making accurate subtractions of this background signal practically impossible during temperature sweeps. And we should be cautious with such subtractions [10]. To eliminate this source of error, we have moved the optics outside the low temperature environment. In this project, both Stanford and Irvine Sagnac fiber-optic heads are located outside optical cryostats with a room temperature optical window between the focusing lens and the sample. The Kerr offset contributed by the optical window due fringing magnetic fields is thus independent of sample temperature, and can be calibrated accurately. One such calibration for the Irvine instrument is illustrated in Fig. 6, using a polished aluminum surface with negligible Kerr effect. The P2 image at T = 3.1 K and B = - 0.34 T shows optical power variations between 7 and 12 μW across the surface, while the Kerr image taken at the same time reveals a spatially uniform Kerr background of 39.7 μrad due to the Faraday effect of the optical window held at 295±0.1 K. And we have verified that it is indeed independent of sample temperature, as shown in Fig. 6(C) (blue). There is a temperature and time-independent instrument offset of 1.6 μrad due to minor misalignment of optics and electronic offsets (Fig. 6(C) (red)). The total offset is thus calibrated to be 1.6 - 112 B μrad, which can be subtracted to produce accurate Kerr values for temperature sweeps (Fig. 2 of the main text) and spatial scans (Fig. 5) even in a magnetic field.

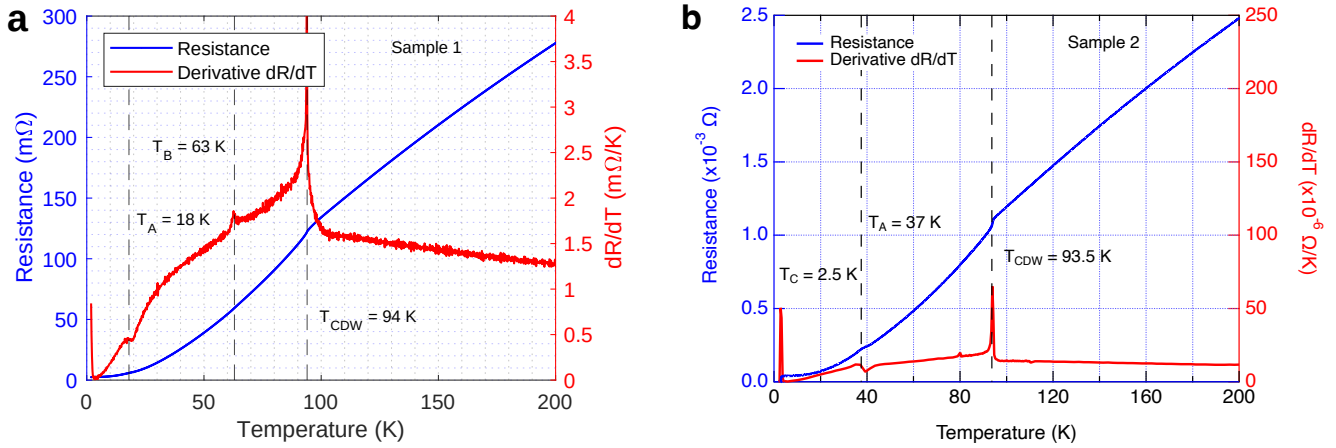

FIG. 7: **DC resistance in CsV_3Sb_5.** **a**, Resistance and derivative dR/dT in CsV_3Sb_5 sample 1. **b**, Resistance and derivative dR/dT in CsV_3Sb_5 sample 2. The charge density transition at T_{CDW} is marked by the kink in the resistance and the pronounced peak in dR/dT. The superconducting transition is marked by the zero resistance below the critical temperature $T_C \approx 2.5$ K. There is an additional feature in dR/dT of a dispersive line shape centered at $T_A \approx 37$ K, which is more pronouced in sample 2.

General Considerations for MO effects

In general Magneto-optical (MO) effects appear because in the presence of magnetism right and left circularly polarized lights propagate differently in solids. When a magnetic field is applied to a diamagnetic insulating solid, magneto-optical effects will originate from the direct effect of the magnetic field on the orbital electronic motion. On the other hand, for ferromagnetic materials, or paramagnetic materials at low temperatures (when their Curie susceptibility is large enough), the effect of the magnetic field on the orbital motion is negligible compared with effects associated with spin-orbit interaction [11]. For simple metals, far from plasma frequency resonances we expect that the main contribution to Kerr response is dominated by off-diagonal intraband Drude-type transitions (i.e. originating from optical conductivity terms $\sigma_{xy}(\omega) = \sigma_0(\omega_c\tau)/[(1 - i\omega\tau)^2 + (\omega_c\tau)^2]$, where $\omega_c = eH/m^*c$ is the cyclotron frequency, σ_0 is the DC Drude conductivity and τ is the scattering time). For example, in Al and Ag [12] and nobel metals including Cu and Au [13] these effects were measured and recently calculated, showing that for energies below ~ 1.5 eV the Kerr rotation is of order $\sim 10^{-9}$ rad/Oe [14]. In the absence of magnetic polarization, the orbital and spin Zeeman terms will contribute off-diagonal terms through interband transitions, which for the above simple metals are at least an order of magnitude smaller. Taking into account optical and transport measurements on CsV_3Sb_5 , both effects are expected to yield an even smaller response, which will not be detectable for the magnetic fields we used with the ZALSI experiments.

DC resistance Measurements

DC resistances measured on sample 1 and sample 2 are shown in Fig. 7. A kink at T_{CDW} is clearly visible in the resistance of both samples, marking the charge density transition. The exact values of T_CDW are determined by the temperatures of the peaks in the first derivative dR/dT curve, and agree with literature data [15] within 1 K. The superconducting transition is marked by the zero resistance below the critical temperature $T_C \approx 2.5$ K. In the dR/dT curve, especially in sample 2, there is an additional feature of a dispersive line shape centered at $T_A \approx 37$ K. We note that NMR experiments [16] have observed a kink behavior at a similar temperature of 35 K in $1/T_1T$, and that the electronic magneto-chiral anisotropy (eMChA) was detected in nonlinear transport [17] below 34 K. Since we observe no spontaneous Kerr signal across T_A, it is suggestive of a phase transition without TRSB at $T_A \approx 37$ K.

[1] J. Xia, P. T. Beyersdorf, M. M. Fejer, and A. Kapitulnik, Applied Physics Letters **89**, 062508 (2006).
[2] G. Sagnac, Comptes Rendus **157**, 708 (1913).
[3] J. Xia, Y. Maeno, P. T. Beyersdorf, M. M. Fejer, and A. Kapitulnik, Phys. Rev. Lett. **97**, 167002 (2006).
[4] E. R. Schemm, W. J. Gannon, C. M. Wishne, W. P. Halperin, and A. Kapitulnik, Science **345**, 190 (2014).
[5] I. M. Hayes, D. S. Wei, T. Metz, J. Zhang, Y. S. Eo, S. Ran, S. R. Saha, J. Collini, N. P. Butch, D. F. Agterberg, A. Kapitulnik, and J. Paglione, Science **373**, 797 (2021).
[6] D. S. Wei, D. Saykin, O. Y. Miller, S. Ran, S. R. Saha, D. F. Agterberg, J. Schmalian, N. P. Butch, J. Paglione,

and A. Kapitulnik, Phys. Rev. B **105**, 024521 (2022).
[7] J. Xia, W. Siemons, G. Koster, M. R. Beasley, and A. Kapitulnik, Phys. Rev. B **79**, 140407(R) (2009).
[8] J. Xia, V. Shelukhin, M. Karpovski, A. Kapitulnik, and A. Palevski, Phys. Rev. Lett. **102**, 087004 (2009).
[9] A. Kapitulnik, Physica B: Condensed Matter **460**, 151 (2015), special Issue on Electronic Crystals (ECRYS-2014).
[10] Y. Hu, S. Yamane, G. Mattoni, K. Yada, K. Obata, Y. Li, Y. Yao, Z. Wang, J. Wang, C. Farhang, J. Xia, Y. Maeno, and S. Yonezawa, "Time-reversal symmetry breaking in charge density wave of CsV_3Sb_5 detected by polar kerr effect," (2022), under Review at Nature Portfolio.
[11] P. S. Pershan, Journal of Applied Physics **38**, 1482 (1967).
[12] E. A. Stern, J. C. McGroddy, and W. E. Harte, Phys. Rev. **135**, A1306 (1964).
[13] J. C. McGroddy, A. J. McAlister, and E. A. Stern, Phys. Rev. **139**, A1844 (1965).
[14] L. Uba, S. Uba, and V. N. Antonov, Phys. Rev. B **96**, 235132 (2017).
[15] B. R. Ortiz, S. M. L. Teicher, Y. Hu, J. L. Zuo, P. M. Sarte, E. C. Schueller, A. M. M. Abeykoon, M. J. Krogstad, S. Rosenkranz, R. Osborn, R. Seshadri, L. Balents, J. He, and S. D. Wilson, Phys. Rev. Lett. **125**, 247002 (2020).
[16] D. Song, L. Zheng, F. Yu, J. Li, L. Nie, M. Shan, D. Zhao, S. Li, B. Kang, Z. Wu, Y. Zhou, K. Sun, K. Liu, X. Luo, Z. Wang, J. Ying, X. Wan, T. Wu, and X. Chen, Science China Physics, Mechanics & Astronomy **65**, 247462 (2022).
[17] C. Guo, C. Putzke, S. Konyzheva, X. Huang, M. Gutierrez-Amigo, I. Errea, D. Chen, M. G. Vergniory, C. Felser, M. H. Fischer, T. Neupert, and P. J. W. Moll, "Field-tuned chiral transport in charge-ordered CsV_3Sb_5," (2022), arXiv:2203.09593 [cond-mat.str-el].